Geophysical Research Letters

RESEARCH LETTER

10.1029/2025GL116952

# ENSO Diversity Explains Interannual Variability of the Pattern Effect

**Robin Guillaume-Castel**[1,2,3], **Paulo Ceppi**[4], **Joshua Dorrington**[2,3], **and Benoit Meyssignac**[1]

[1]LEGOS, Université de Toulouse, CNES, CNRS, IRD, UPS, Toulouse, France, [2]Geophysical Institute, University of Bergen, Bergen, Norway, [3]Bjerknes Center for Climate Research, Bergen, Norway, [4]Imperial College London, London, UK

**Key Points:**

- We apply dimensionality reduction to identify dominant modes of Pacific sea surface temperature (SST) variability linked with the pattern effect
- Eastern Pacific and Modoki El Niño-Southern Oscillation dominate the interannual pattern effect but their contributions have opposite sign
- Considering El Niño-Southern Oscillation diversity is key to study how SST variability impacts the Earth energy budget

**Supporting Information:**

Supporting Information may be found in the online version of this article.

**Correspondence to:**

R. Guillaume-Castel,
robin.guillaume-castel@uib.no

**Citation:**

Guillaume-Castel, R., Ceppi, P., Dorrington, J., & Meyssignac, B. (2025). ENSO diversity explains interannual variability of the pattern effect. *Geophysical Research Letters*, *52*, e2025GL116952. https://doi.org/10.1029/2025GL116952

Received 14 MAY 2025
Accepted 22 SEP 2025

**Author Contributions:**

**Conceptualization:** Robin Guillaume-Castel, Paulo Ceppi, Benoit Meyssignac
**Data curation:** Robin Guillaume-Castel
**Formal analysis:** Robin Guillaume-Castel
**Funding acquisition:** Benoit Meyssignac
**Investigation:** Robin Guillaume-Castel, Paulo Ceppi, Joshua Dorrington, Benoit Meyssignac
**Methodology:** Robin Guillaume-Castel, Paulo Ceppi, Joshua Dorrington, Benoit Meyssignac
**Visualization:** Robin Guillaume-Castel
**Writing – original draft:** Robin Guillaume-Castel
**Writing – review & editing:** Robin Guillaume-Castel, Paulo Ceppi, Joshua Dorrington, Benoit Meyssignac

## Abstract

The spatial pattern of sea surface temperature (SST) affects the global radiative budget through the “pattern effect.” While previous studies highlighted the role of El Niño–Southern Oscillation (ENSO) in unforced pattern effect, a systematic assessment of the dominant modes of SST variability for the top of atmosphere energy budget has been lacking. Using Partial Least Squares Regression, we identify Eastern Pacific and Modoki ENSO as the two leading modes most relevant to the pattern effect at interannual timescales. These ENSO variants exhibit distinct radiative signatures due to subtle shifts in the location of SST anomalies relative to the climatological warm pool. Furthermore, analysis of individual ENSO events indicates that each event has a unique radiative signature depending on its evolving spatial structure. These findings highlight the importance of accounting for ENSO diversity to accurately understand how modes of SST variability influence the global energy budget.

## Plain Language Summary

Our climate warms because the Earth receives more energy from the Sun than it can send back into space. How much energy the planet can release depends mostly on surface temperatures, and especially on how much warmer the eastern Pacific (EP) is compared to the western Pacific. This temperature difference varies with climate change, but also changes naturally through recurring climate patterns, or “modes,” that shift sea surface temperatures in different regions. The most important of these in the Pacific is the El Niño–Southern Oscillation (ENSO), which affects the entire tropical Pacific on a cycle every 3–5 years. In this study, we used a statistical method to test whether ENSO is the most important mode for understanding how natural changes in surface temperature affect the Earth's energy balance. We found that two types of ENSO–one centered in the EP and another in the central Pacific–have the strongest impact. These two patterns affect the planet's energy differently because of how they affect temperatures near Indonesia, where the ocean is typically warmest. This means we need to consider the diversity of ENSO events to fully understand how ocean temperature changes influence the global climate.

## 1. Introduction

The global top of atmosphere (TOA) radiative budget is linked to the evolution of global mean surface temperature (GMST) through radiative feedbacks. Beyond the global mean, the pattern of sea surface temperature (SST) also affects this energy budget through what is called the “pattern effect” (Stevens et al., 2016). Following Ceppi and Fueglistaler (2021), Meyssignac, Guillaume-Castel, and Roca (2023) and Guillaume-Castel and Meyssignac (2025), we define the pattern effect as the component of global TOA radiative anomalies attributable to deviations in the spatial distribution of SST from its global-mean. This quantity is a radiative flux in W $m^{-2}$. All TOA fluxes are given positive down.

A growing body of literature has studied the pattern effect to better understand how the planet responds to radiative forcing (e.g., Andrews & Webb, 2018; Armour, 2017). Indeed, the pattern effect is critical for accurately quantifying the rate of global transient warming (Alessi & Rugenstein, 2023; Armour et al., 2024; Dong et al., 2021; Guillaume-Castel & Meyssignac, 2025) and future long-term warming, such as equilibrium climate sensitivity or committed warming (Armour, 2017; Sherwood et al., 2020; Zhou et al., 2021). The pattern effect can however occur even in the absence of an external forcing. Evidence of such an unforced pattern effect (Dessler, 2020) was found in climate model simulations (Davis et al., 2024; Lutsko & Takahashi, 2018; Proistosescu et al., 2018; Tsuchida et al., 2023) and observations (Ceppi & Fueglistaler, 2021; Chao et al., 2022; Fueglistaler, 2019; Meyssignac, Chenal, et al., 2023). On interannual timescales, El Niño–Southern Oscillation

(ENSO) has emerged as a key driver of pattern effect variability (Ceppi & Fueglistaler, 2021; Dessler, 2020; Lutsko & Takahashi, 2018; Tsuchida et al., 2023), due to its strong influence on the SST gradient in the tropical Pacific, the main ocean basin associated with the pattern effect (Dong et al., 2019; Zhou et al., 2017). On longer timescales, the Pacific Decadal Oscillation (PDO), a low-frequency ENSO-related mode, has also been associated with the pattern effect in historical observations (Loeb, Thorsen, et al., 2018; Meyssignac, Chenal, et al., 2023). While the Pacific appears to be dominant, modes of variability in other ocean basins, such as the Atlantic Multidecadal Oscillation (Dessler, 2020), and low-frequency modes of the global ocean (Wills et al., 2021), may also contribute to this pattern effect.

No systematic assessment of the relative contributions of different modes of SST to the unforced pattern effect has been undertaken to date. While the Pacific ocean has been highlighted as dominant for the pattern effect (Dong et al., 2019; Zhou et al., 2017), it remains unclear from the literature whether ENSO truly dominates the unforced pattern effect in the Pacific, or if other modes may play a comparable or greater role. Notably, different ENSO variants, such as Eastern Pacific (EP), Central Pacific (CP) and Modoki ENSOs (Ashok et al., 2007; Kao & Yu, 2009; Takahashi et al., 2011) have different spatial patterns of SST anomaly, which may in turn produce different pattern effects. To address this gap, we follow an objective dimensionality reduction approach to identify which modes of SST variability most strongly affect the TOA energy budget through the pattern effect, focusing on the Pacific Ocean at interannual timescales.

## 2. Data and Methods

### 2.1. Dimensionality Reduction Approach

We analyze three monthly observational SST data sets: HadiSST (Titchner & Rayner, 2014), ERSSTv5 (Huang et al., 2017a) and COBE2 (Ishii et al., 2005). While these products provide data back to 1850, we constrain our analysis to the period 1960–2024, which has an increased observational coverage and overall more reliable SST data sets. The SST data are regridded onto a common 2° × 2° grid (the resolution of ERSSTv5). We compute SST anomalies (SSTA) by removing the monthly climatology and the 1960–1980 mean value for each grid point. As we focus on spatial variability, the global mean SSTA is also removed from each grid point. Additionally, we remove a potential long term forced signal by subtracting a linear trend fitted to each grid point time series over the study period.

We follow a dimensionality reduction approach which consists in approximating the SSTA field by a sum of $N$ standardized patterns $P_k$ at each location $x$, multiplied by standardized time series $\theta_k$ at each time $t$ and amplitudes $\phi_k$, such that

$$\mathrm{SSTA}(x,t) \approx \sum_{k=1}^{N} \phi_k P_k(x)\theta_k(t), \tag{1}$$

where the spatial variance of $P_k(x)$ is 1 and the temporal variance of $\theta_k(t)$ is also 1. Note that we arbitrarily choose the mode orientations such that they fit known physical modes best.

We use two different, but related, dimensionality reduction methods: empirical orthogonal function (EOF) analysis and partial least squares regression (PLSR, Abdi, 2010; scikit-learn, 2025). Both algorithms aim to capture as much of a certain kind of variance as possible within a lower dimensional space. For EOF analysis, the aim is to maximize the temporal variance explained by the data as captured by the covariance matrix. This produces, by construction, both patterns and components that are mutually orthogonal to each other. PLSR is a direct extension of EOF analysis that aims to maximize the cross-covariance explained between the predictor data set $X$, which is being reduced in dimension, and a predictand data set $Y$. In this case the components are mutually orthogonal but the patterns are not. PLSR is also closely related to canonical correlation analysis, but maximizing cross-covariance rather than cross-correlation. On a high level, EOFs aim to capture as much variability as possible within a data set, while PLSR aims to capture predictive variability that explains variance in a separate target variable.

To ensure that the leading EOFs are relevant to the pattern effect, the SSTA are first weighted by radiative Green's functions (GFs), which correspond to the sensitivity of the global TOA radiative budget to local SST changes. Extensive details about the protocole to obtain these GFs are given in the Green's Functions Model

Intercomparison Project (GFMIP) reference paper (Bloch-Johnson et al., 2024). The weighting is applied by performing the dimensionality reduction on the GF-weighted SSTA, that is, GF($x$) × SSTA($x$), and then dividing the resulting modes at each grid point by the local GF($x$) to get equivalent SSTA components. This process allows us to highlight areas where SSTA variability has a substantial global radiative impact (either through large variability in SSTA itself, or through a large weighting by the GF). As a target predictand for PLSR, we construct a timeseries representing the influence of non-uniform warming in the Pacific ocean, that is, different patterns of warming, on the global radiation budget. We denote this quantity $R_P$, called the Pacific-induced radiative response to non-uniform warming by Meyssignac, Guillaume-Castel, and Roca (2023) (see also Bloch-Johnson et al., 2024; Guillaume-Castel & Meyssignac, 2025; Zhang et al., 2023):

$$R_P(t) = \sum_{x \in \text{Pacific}} \text{SSTA}(x,t) \times \text{GF}(x). \tag{2}$$

We use GFs from six different climate models collected in the Green's Functions Model Intercomparison Project (GFMIP, Bloch-Johnson et al., 2024): CAM4 (Dong et al., 2019), CAM5 (Zhou et al., 2017), HadCM3 (Bloch-Johnson et al., 2024), GFDL-CM4 (Zhang et al., 2023), CanESM5 (Bloch-Johnson et al., 2024) and ECHAM6 (Alessi & Rugenstein, 2023). All GFs are also conservatively regridded to a 2° × 2° grid. Additionally, we use a "mean" GF computed as the mean of all different GFs. Hereafter we denote any combination of one GF and one SST product as a member, and the set of all members is referred to as the ensemble. Overall, our ensemble consists of 21 members. We confirm the dominance of the Pacific Ocean by computing the variance of $R_P$ for all major ocean basins separately and comparing it to $R_P$ computed on the global oceans (see Figure S1 in Supporting Information S1). We find that the Pacific always shows the highest variance, with an average of $\tilde{7}0\%$ of the global ocean $R_P$ variance, while other ocean basins never exceed 18%.

### 2.2. Evaluation of the Dimensionality Reduction Skill

#### 2.2.1. Comparison With Physical Variability Modes

We compare our patterns with known physical modes in the Pacific Ocean. Since the main mode of variability in the Pacific Ocean is ENSO, we will compare our results with the Niño3.4 index ($N_{34}$), representative of the canonical ENSO mode, but also three additional indices that distinguish between different flavors of ENSO: $N_{\text{EP}}$ and $N_{\text{CP}}$, defining EP and CP ENSO (called $N_{\text{CT}}$ and $N_{\text{WP}}$ by Ren & Jin, 2011), and $N_M$ representing ENSO Modoki (Ashok et al., 2007; Takahashi et al., 2011). $N_{34}$ is defined as the mean temperature anomaly in the region 5°N–5°S, 170°W–120°W. $N_{\text{EP}}$ and $N_{\text{CP}}$ are then computed based on the Niño3 ($N_3$) and Niño4 ($N_4$) indices. $N_3$ and $N_4$ are the mean SSTA in the (5°N–5°S, 150°W–90°W) and (5°N–5°S, 160°E−150°W) regions respectively. $N_{\text{EP}}$ and $N_{\text{CP}}$ are defined as

$$\begin{cases} N_{\text{EP}} = N_3 - \alpha N_4 \\ N_{\text{CP}} = N_4 - \alpha N_3 \\ \alpha = \begin{cases} 2/5 & \text{if } N_3 N_4 > 0 \\ 0 & \text{otherwise} \end{cases} \end{cases} \tag{3}$$

$N_{\text{M}}$ is defined as the timeseries of the second EOF of tropical Pacific SST, confined to 10°S−10°N (Takahashi et al., 2011). Following Takahashi et al. (2011), all timeseries are smoothed using a 1-2-1 filter and standardized. The EOF and PLSR timeseries are also smoothed with the same filter.

We determine an associated SSTA pattern for each index as the slope of the linear regression between the index and the SSTA field (Figure 1g–1i). The similarity of the $P_k$ to these modes of variability is assessed by computing the temporal correlation of the timeseries and the spatial correlation of the SSTA patterns.

#### 2.2.2. Contribution to the Pattern Effect

We evaluate the contribution of each pattern to the pattern effect by computing an associated radiative response to non-uniform warming $R_{P,k}$:

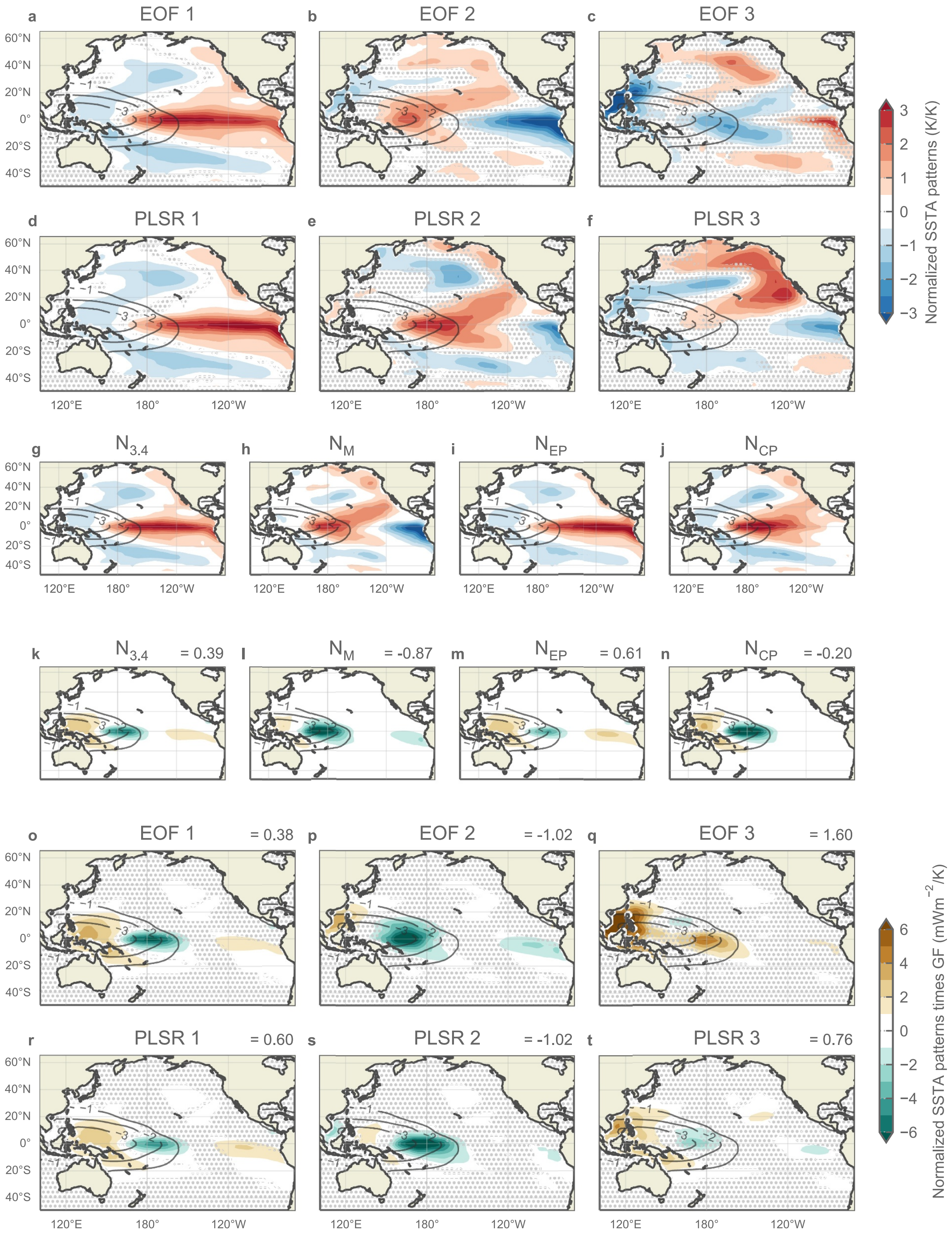

**Figure 1.** Normalized ensemble mean leading SSTA patterns for EOFs (a–c) and partial least squares regression (PLSR) (d–f). SSTA patterns associated with the ENSO indices are included for comparison (g–j). Equivalent SSTA × GF components for ENSO indices (k–n), EOFs (o–q) and PLSR (r–t). The pattern effect efficiency Π is displayed in W m$^{-2}$ K$^{-1}$. Gray contours indicate the mean Green's function (GF) with levels in mW m$^{-2}$ K$^{-1}$. Panels (k–t) are equivalent to panels (a–j) multiplied by the GF. In panels (a–f) and (o–t), stippling indicates where less than 90% of members (i.e., fewer than 19/21) agree on the sign of the feature.

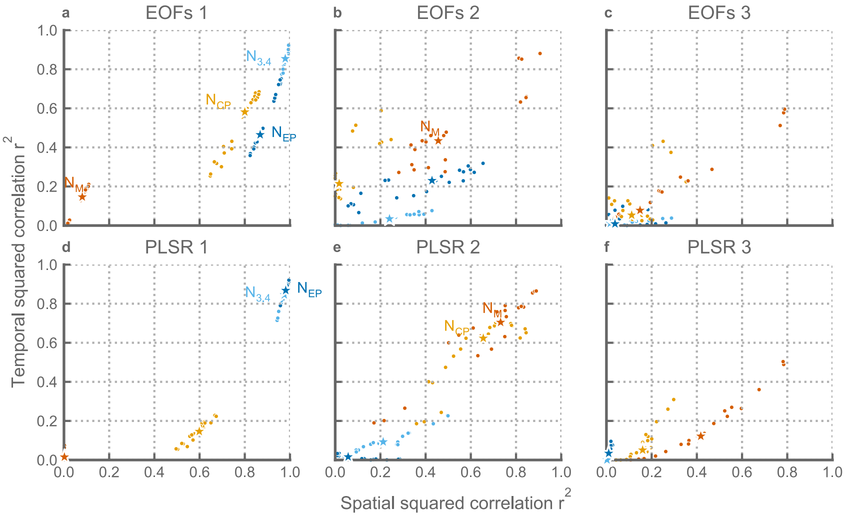

**Figure 2.** Comparison between ENSO indices and leading modes of EOFs (a–c) and partial least squares regression (d–f). The *x*-axis shows the squared spatial correlation and the *y*-axis the squared temporal correlation. Each color represents one index. Dots represent individual members and stars show the median scores obtained for the ensemble.

$$R_{P,k}(t) = \phi_k \left( \sum_{x \in \text{Pacific}} P_k(x) \times \text{GF}(x) \right) \theta_k(t) = \phi_k \Pi_k \theta_k(t). \tag{4}$$

We call $\Pi$ the pattern effect efficiency, which corresponds to how well the SST variance of a given mode of variability is communicated to the global TOA through the pattern effect. The larger $\Pi$, the greater the associated pattern effect per K of SSTA amplitude of variability. It is in units of W m$^2$ K$^{-1}$. In practice, the pattern effect efficiency is mainly set by the degree to which each mode projects onto the climatological warm pool as this is where the GFs are the most sensitive (Dong et al., 2019). In addition to the correlations mentioned in Section 2.2.1, we evaluate the pattern effect efficiency for the ENSO indices, providing an additional benchmark for comparison with our leading modes. We then quantify the variance ratio between $R_{P,k}$ and $R_P$. With $\sigma$ the standard deviation, this ratio is

$$\frac{\sigma(R_{P,k})^2}{\sigma(R_P)^2} = \left( \frac{\phi_k \Pi_k}{\sigma(R_P)} \right)^2. \tag{5}$$

Since the time series of the successive modes are orthogonal by design, this corresponds to the variance of $R_P$ explained by $R_{P,k}$. The dimensionality reduction is successful if $R_P$ is well approximated by $R_{P,k}$ of the first few modes, with improving performance as additional modes are included. We focus on the three leading modes, but also quantify the variance explained by the first $k$ leading modes (up to 10) to compare both methods.

## 3. Results

### 3.1. Description of the Leading Modes

The patterns determined from EOF analysis and PLSR are presented in Figure 1, along with ensemble mean pattern effect efficiencies and the patterns associated with the ENSO indices. The spatial and temporal correlations of the EOF and PLSR modes with the ENSO indices are shown in Figure 2. SSTA patterns for individual members are presented in Figure S2 in Supporting Information S1 for EOFs and Figure S3 in Supporting Information S1 for PLSR, and individual $r^2$ values for all members are presented in Tables S1–S6 in Supporting Information S1. Additionally, we reproduced our analysis and Figure 1 with the global ocean (Figure S4 in Supporting Information S1). We confirm that the leading EOFs and PLSR modes are qualitatively similar to the ones determined with the Pacific ocean only, emphasizing its dominance in the internal variability of the pattern effect.

### 3.1.1. EOFs

The leading EOF of GF-weighted SSTA (Figure 1a) shows a canonical ENSO-like pattern and is highly consistent with $N_{3.4}$ (Figure 1g, Figure 2a), with a temporal $r^2$ of 0.85 and a spatial $r^2$ of 0.98 (All correlations are given as ensemble median $r^2$; values for individual members can be found in Figure 2). This mode is robust across the ensemble. Depending on individual members, EOF1 is also well correlated with $N_{\mathrm{EP}}$ or $N_{\mathrm{CP}}$ in both time and space: members with GFs from CanESM5, GFDL-AM4 and HadCM3 show stronger correlations with $N_{\mathrm{EP}}$ while the others show stronger correlations with $N_{\mathrm{CP}}$. As Niño3.4 correlates with both $N_{\mathrm{EP}}$ and $N_{\mathrm{CP}}$ (Ren & Jin, 2011), this is consistent with EOF1 being equivalent to the canonical ENSO (as represented by the Niño3.4 index). A positive EOF1 phase leads to a positive (i.e., downward) contribution to global TOA radiative anomaly from SSTs north of the maritime continent, and a negative contribution coming from a region, narrower in latitude, eastwards into the CP (Figure 1j). Even though the negative contribution has a higher amplitude, the areal extent of the positive contribution is greater. EOF1 has, on average, a moderate pattern effect efficiency with $\Pi = 0.38$ W m$^{-2}$ K$^{-1}$, consistent with $N_{3.4}$ (0.39 W m$^{-2}$ K$^{-1}$).

EOF2 (Figure 1b) most notably shows a strong negative SSTA in the EP and a positive SSTA in the western Pacific. Both lead to an important negative global TOA radiative anomaly, with little positive compensation in the western Pacific. This EOF modulates the western extension and the EP anomalies of the canonical ENSO as captured by EOF1. This pattern is similar to El Niño Modoki with moderate spatial and temporal $r^2$ (0.46 and 0.44 respectively). Substantial correlation ($r^2 > 0.5$ in both space and time) was only found for six members coming from two GFs (HadCM3 and CanESM5). While the spatial patterns are roughly consistent within the ensemble (see Figure S2 in Supporting Information S1), the exact locations of positive and negative anomalies make EOF2 less robust than EOF1 regarding the pattern effect. The weighted EOF analysis of the total Pacific appears to be consistent with an EOF decomposition of the tropical Pacific only (Takahashi et al., 2011), highlighting how the tropics play a key role in the pattern effect. EOF2 has a pattern effect efficiency three times higher than EOF1, and of opposite sign.

EOF3 (Figure 1c) shows some CP cooling resembling Niño CP and Modoki, as well as around the maritime continent, leading to an average pattern effect efficiency of $\Pi = 1.60$ W m$^{-2}$ K$^{-1}$. This mode is not robust across the ensemble (see Figure S2 in Supporting Information S1) and does not robustly correlate with Niño indices. Still, the visual similarity with $N_{\mathrm{M}}$ is reflected in substantial spatial correlation and moderate temporal correlation with a few individual members (from the GFDL-AM4 GFs, see Figure 2c and Table S3 in Supporting Information S1).

### 3.1.2. PLSR

PLSR1 and PLSR2 are consistent with physical modes of variability. representing EP ENSO (PLSR1) and a mix between CP ENSO and Modoki (PLSR2, Figures 1h and 1i). Compared to EOF1, PLSR1 also correlates well with $N_{3.4}$. It is however much better related with $N_{\mathrm{EP}}$ than EOF1, with a spatial $r^2$ of 0.98 and a temporal $r^2$ of 0.87 (Figure 2d), and only spatially related to $N_{\mathrm{CP}}$ ($r^2 = 0.60$). While EOF1 could be considered equivalent to the canonical ENSO, this indicates that PLSR1 primarily comprises the East Pacific contributions of ENSO, which still correlates well with $N_{3.4}$ (Ren & Jin, 2011). This is a robust feature across the ensemble. We verify that PLSR1 is closer to $N_{\mathrm{EP}}$ than EOF1 by plotting the differences in pattern between PLSR1 minus EOF1 (Figure S5a in Supporting Information S1) and $N_{\mathrm{EP}}$ minus $N_{3.4}$ (Figure S5b in Supporting Information S1). Compared to EOF1, PLSR1 notably shows a reduced amplitude in the CP (consistent with the difference between $N_{\mathrm{EP}}$ and $N_{3.4}$) leading to a weaker negative contribution to the TOA energy budget. This results in a slightly higher pattern effect efficiency of $\Pi = 0.60$ W m$^{-2}$ K$^{-1}$, meaning that for the same SSTA amplitude, PLSR1 leads to a pattern effect roughly 60% stronger than EOF1, which is consistent with the pattern effect efficiency of $N_{\mathrm{EP}}$ (0.61 W m$^{-2}$ K$^{-1}$).

PLSR2 (Figure 1d) shows a characteristic CP warming consistent with both $N_{\mathrm{CP}}$ and $N_{\mathrm{M}}$ (compare with Figures 1h and 1i) and substantial correlation with both indices, although the correlation with $N_{\mathrm{M}}$ is slightly higher with a spatial $r^2$ of 0.73 (0.66 for $N_{\mathrm{CP}}$) and a temporal $r^2$ of 0.70 (0.62 for $N_{\mathrm{CP}}$, Figure 2e). The SSTA in the central tropical Pacific is shifted to the west compared to canonical ENSO, and occurs in a region with only negative radiative sensitivity. This is consistent across most of the ensemble, although GFs from GFDL-AM4 and HadCM3 show weaker $r^2$ with $N_{\mathrm{CP}}$ and $N_{\mathrm{M}}$ at around 0.2 to 0.4 (see Table S5 in Supporting Information S1). PLSR2 has a stronger average pattern effect efficiency than PLSR1 and of the opposite sign of $\Pi = -1.02$ W m$^{-2}$ K$^{-1}$, which is more

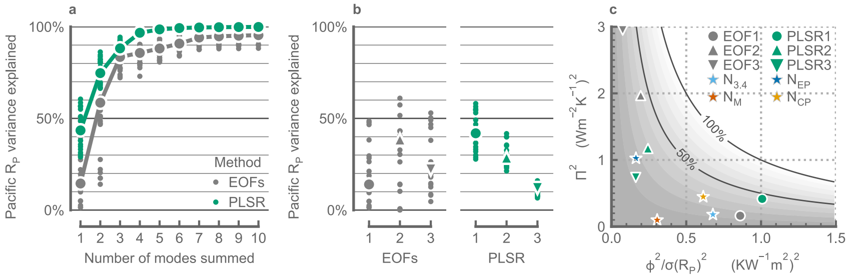

**Figure 3.** (a, b) Percent of $R_P$ variance explained by the sum of the first N modes (a) and by each of the 3 leading modes (b). Smaller dots represent individual members and bigger dots are the ensemble mean. (c) Squared pattern effect efficiency $\Pi^2$ against squared scaled amplitude of variability $\phi^2/\sigma(R_P)^2$ for the first three modes of each method (ensemble means only). The same metrics were computed for the ENSO indices and are displayed as stars. Shaded contours show every 10% of explained variance, calculated as the product of the *x*- and *y*-axes (Equation 5).

consistent with $N_{\mathrm{M}}$ ($-0.87$ W m$^{-2}$ K$^{-1}$) than $N_{\mathrm{CP}}$ ($-0.20$ W m$^{-2}$ K$^{-1}$). The higher correlations and the closer pattern effect efficiency makes PLSR2 more similar to $N_{\mathrm{M}}$ than to $N_{\mathrm{CP}}$. These results indicate that ENSO Modoki likely has a strong influence on the pattern effect.

Finally, PLSR3 (Figure 1f) shows a strong North Pacific signal, robust across the ensemble, which could be related to the PDO. A temporal $r^2$ of 0.27 was found between PLSR3 and the PDO after applying a 10-year low pass filter but no spatial correlation was found. As for EOF3, some members show substantial spatial and moderate temporal $r^2$ (coming from GFDL-AM4 and HadAM3 GFs).

### 3.2. Contribution of Each Mode to the Pattern Effect

We now assess the contribution of each identified mode to the pattern effect. For each of the two methods used, we first compute the share of the $R_p$ variance explained by the first *k* modes (Figure 3a). Then, we compute the share of the $R_p$ variance explained by each of the first three modes to evaluate which modes are dominant (Figure 3b). Finally, we interpret the variance explained by the pattern effect efficiency Π and by the amplitude of each mode scaled by the $R_P$ standard deviation, $\phi/\sigma(R_P)$, following Equation 5 (Figure 3c).

The first three EOFs robustly explain approximately 80% of the total variance with some disparity across members (Figure 3a). The first six modes are required to reach 90%. EOF1 explains on average only 14.0% of the total $R_P$ variance (Figure 3b), even though EOF1 has the highest amplitude $\phi$ by design. The reduced pattern effect efficiency strongly dampens its radiative impact (Figure 3c). We find a pattern effect efficiency of 0.39 W m$^{-2}$ K$^{-1}$ for Niño3.4, equivalent to EOF1, which confirms that it has a limited radiative signature through the pattern effect. EOF2, despite having a smaller amplitude $\phi$ (0.12 instead of 0.27 on average), leads to a stronger TOA radiative anomaly because of a much stronger pattern effect efficiency (in absolute terms, 1.02 instead of 0.38). EOF2 explains the most of the $R_P$ variance with 38.5%. EOF3 spans slightly more variance than EOF1 with 22.2%, but its amplitude is smaller and its pattern effect efficiency higher. For a few members however, EOF3 can explain up to 70% of the $R_P$ variance (outliers in Figure 3b). Overall, the EOF method shows limited robustness across ensemble members.

PLSR identifies modes that maximize their covariance with $R_P$. Consequently, the resulting modes perform better at explaining the $R_P$ variance. The variance explained is much more consistent across the ensemble than with EOFs (smaller spread in Figures 3a and 3b). The first three PLSR modes jointly explain an average of 88% of the $R_P$ variance, while the first six modes explain 99% (Figure 3a). PLSR1 explains an average of 41.9% of the $R_P$ variance, while PLSR2 explains 28.6% on average. This suggests that EP and Modoki ENSO, taken individually, have a substantial global radiative signature through the pattern effect.

Finally, PLSR3 explains much less than the two first modes (12.0%). Overall, the PLSR method is more robust than EOF analysis and is well suited to our study, as it extracts robust physical modes which explain a substantial fraction of the pattern effect variance.

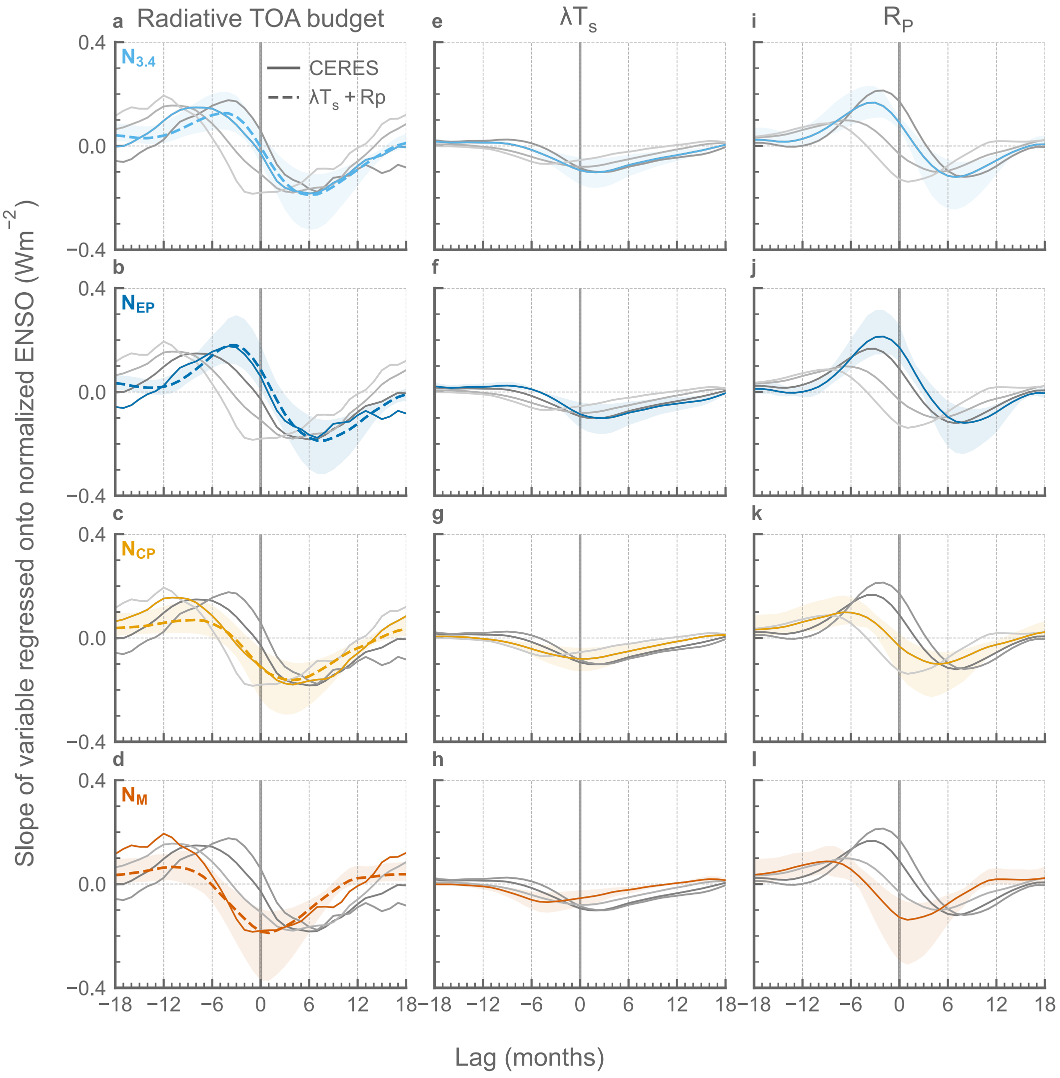

**Figure 4.** Slope of the linear regression between ENSO indices ($x$) and global top of atmosphere (TOA) radiation time series ($y$). All curves show ensemble-mean results. Each row represents one ENSO index in color with the uncertainty denoted by quantiles 5%–95%. The gray lines show the other ENSO indices for reference. (a–d). Observed TOA radiation imbalance from CERES-EBAF (solid) and from the sum of global-mean surface temperature contribution and pattern effect (dashes). Gray lines only show CERES. (e–h). TOA radiation imbalance caused by global surface temperature change anomalies only. (i–l). TOA radiation imbalance caused by the pattern effect. Negative lags mean that the radiative anomalies lead the ENSO anomalies, and vice versa.

### 3.3. The Different Radiative Signatures of ENSO Indices

Our results so far demonstrate that different flavors of ENSO have different radiative signatures associated with the pattern effect. Notably, $N_{EP}$ and $N_M$ have a stronger pattern effect than $N_{3.4}$ and $N_{CP}$. In addition, the global radiative contributions of these three variants have different sign: while positive $N_{3.4}$ and $N_{EP}$ lead to a positive TOA radiative anomaly from the pattern effect, $N_{CP}$ and $N_M$ have a negative pattern effect.

To validate these findings, we regress the global TOA energy imbalance $N$ from the CERES-EBAF 4.2.1 observational product (Loeb, Doelling, et al., 2018) onto the ENSO indices. All regressions are computed after removing the trend and climatology over the CERES period (2001–2024). As SSTA patterns evolve during the ENSO cycle, different radiative signatures are expected at different times across the cycle. Following Ceppi and Fueglistaler (2021), we compute lagged-regressions from −18 to +18 months (Figure 4a).

Physically, a positive slope means that a positive phase of ENSO is associated with a positive global TOA radiative anomaly and vice versa. The lagged regression with CERES shows a sinusoidal oscillation for all indices, with mostly positive slopes at negative lags and negative slopes at positive lags. $N$ anomalies peak at 0.2 W $\mathrm{m}^{-2}$ $\mathrm{K}^{-1}$ 6 months before the peak of $N_{3.4}$ cycle. The slope then decreases and crosses the 0-line at the peak of the cycle. This means that when only considering instantaneous regressions, $N_{3.4}$ has no global radiative signature. The slope then turns negative, with a minimum peaking around $-0.2$ W $\mathrm{m}^{-2}$ $\mathrm{K}^{-1}$ reached after 6 months. These results are consistent with Xie et al. (2016), Fueglistaler (2019) and Ceppi and Fueglistaler (2021), although the magnitude of the anomalies is reduced compared to Ceppi and Fueglistaler (2021), because we consider global-mean $N$ instead of tropical-mean. $N_{\mathrm{EP}}$, $N_{\mathrm{CP}}$ and $N_{\mathrm{M}}$ show a similar behavior, but with slightly different timings and amplitudes: the $N_{\mathrm{EP}}$ cycle is shifted toward more positive lags, and as a result the radiative anomalies are positive at lag 0; the opposite is true of $N_{\mathrm{CP}}$ and $N_{\mathrm{M}}$.

ENSO can affect the global TOA energy imbalance either through GMST changes, or through the pattern effect as the SSTA pattern evolves. To estimate each contribution, we regress the GMST anomalies from the HadCRUT5 product (Morice et al., 2021) as well as the global $R_P$ (Equation 1) onto the ENSO indices. Our previous analysis was based on the radiative impact of Pacific SSTA only. However, as ENSO can covary with SSTA in the Indian or the Atlantic oceans, we compute $R_P$ for the global ocean to account for all pattern effect associated with ENSO, giving slightly different values $\left(r^2 = 0.82\right)$. To quantify the radiative impact of GMST change during ENSO, the slope of the linear regression between the ENSO indices and GMST is multiplied by the best estimates of the global climate feedback parameter from the IPCC AR6 assessment ($\lambda = -1.16\ [-1.81,\ -0.51]$ W $\mathrm{m}^{-2}$ $\mathrm{K}^{-1}$, mean and 5th–95th quantiles, Forster et al., 2021).

The dependence of the global energy budget on ENSO is mainly explained by the pattern effect (Figure 4c), while the GMST contribution is smaller (Figure 4b), again in agreement with Ceppi and Fueglistaler (2021). The slopes of the linear regression between the indices and $R_P$ (Figure 4c) at lag 0 are consistent with our analysis in 3.2, with a limited positive pattern effect of $N_{3.4}$ (our EOF1), a stronger positive pattern effect of $N_{\mathrm{EP}}$ (PLSR1), a limited negative pattern effect of $N_{\mathrm{CP}}$ and a stronger negative one for $N_{\mathrm{M}}$ (PLSR2).

We verify our approach by summing the slopes from the two contributions (GMST change and pattern effect) and comparing it to the total slope against CERES (Figure 4a). Although the radiative anomalies are underestimated for $N_{\mathrm{CP}}$ and $N_{\mathrm{M}}$ before lag $-6$, the overall global TOA radiative response to ENSO modes is well explained by the sum of the contributions from GMST change and from the pattern effect for all indices, particularly at lags $-6$ to $+6$.

This analysis highlights that, while different types of ENSO may exhibit superficially similar SSTA patterns, subtle differences in the location of the warm and cold anomalies relative to the climatological warm pool result in very different global radiative signatures across their cycle through the pattern effect.

## 4. Summary and Conclusion

We applied dimensionality reduction methods to the SSTA field to determine the dominant modes of Pacific SST variability associated with the pattern effect at interannual timescales. By comparing EOF analysis and PLSR, we showed that PLSR provides a more effective framework for identifying these modes. The results are more robust across a range of SST products and Green's Functions (GF), and it provides a better reconstruction of the global TOA radiative response to non-uniform warming with fewer modes.

Using PLSR, we identified two known modes of SST variability with large contributions to interannual global TOA radiative anomalies: Eastern Pacific (EP) and Modoki ENSO. These findings confirm the importance of ENSO in understanding the internal variability of the pattern effect (Ceppi & Fueglistaler, 2021; Lutsko & Takahashi, 2018; Tsuchida et al., 2023). Although they may look somewhat similar to the canonical ENSO, subtle shifts in the location of the positive and negative SST anomalies have a large impact on their overlap with the GF and thus on the net global radiative response. As a result, Modoki and EP ENSO have opposite-signed global radiative impacts. This highlights that the diversity of ENSO spatial structures is critical to quantifying the unforced pattern effect.

Importantly, our results indicate that the canonical $N_{3.4}$ index is insufficient to fully understand the global radiative signature of ENSO. By aggregating different ENSO types into a single index, it masks the distinct radiative signatures associated with different spatial structures. We argue that there is not a unique "ENSO pattern effect" (as in Ceppi & Fueglistaler, 2021): instead, each ENSO event produces a different radiative response depending on the temporal evolution of its SST pattern. In reality, CP, Modoki, canonical and EP ENSO are not strictly separated, and the indices used in this study may represent different stages of the same events (Capotondi et al., 2020). Figure S6 in Supporting Information S1 shows the evolution of $N_{\mathrm{EP}}$ and $N_{\mathrm{CP}}$ for selected ENSO years. It shows that some events are only represented by one type of ENSO (the 2009 El Niño is mostly CP; the 2017 La Niña is only EP), while others exhibit a cycle with evolving SST patterns (e.g., 2007 La Niña and 2023 El Niño).

ENSO diversity has been evolving in the historical period (Dieppois et al., 2021) and is projected to change in future climates (Geng et al., 2022). The impact of ENSO on global TOA anomalies in the satellite record may not be representative of future climate change. Since many climate models struggle to reproduce the diversity and impacts of Modoki, CP and EP ENSO events (e.g., Hou & Tang, 2022), this may limit their ability to accurately simulate present and future unforced variability in the pattern effect.

The key limitation of this study is that we use GFs derived from climate models, which may deviate from the real-world sensitivity of the radiation budget to local SST changes. Notably, models underestimate the EP low cloud response to warming in the Indo-Pacific warm pool (Ceppi et al., 2024). While ongoing research aims at estimating such sensitivity using observational data (Rugenstein et al., 2025; Van Loon et al., 2025), there is no consensus on the methodology yet. Despite this limitation, PLSR provides a promising framework for future research into a broader spectrum of pattern effect variability, including other ocean basins such as the Atlantic (following Dessler, 2020) or longer timescales to better understand lower-frequency contributions to the pattern effect (Loeb, Thorsen, et al., 2018; Meyssignac, Chenal, et al., 2023).

## Conflict of Interest

The authors declare no conflicts of interest relevant to this study.

## Data Availability Statement

All SST data sets and GFs used in this work are publicly available. HadiSST can be downloaded from the UK Met Office website at https://www.metoffice.gov.uk/hadobs/hadisst/data/HadISST_sst.nc.gz. COBE2 data set is available at https://psl.noaa.gov/data/gridded/data.cobe2.html and ERSSTv5 can be accessed on NOAA's website (Huang et al., 2017b). The CERES-EBAF data used are available at https://ceres.larc.nasa.gov/data/. HadCRUT5 data are available at https://www.metoffice.gov.uk/hadobs/hadcrut5/data/HadCRUT.5.0.2.0/download.html. Green's functions collected in the GFMIP can be found on the GFMIP github page https://github.com/GFMIP/preliminary_spatial_feedbacks. During the analysis, the Pacific Ocean is extracted by using mask provided by the RECCAP2-ocean project available at https://github.com/RECCAP2-ocean/R2-shared-resources/blob/master/data/regions/RECCAP2_region_masks_all_v20221025.nc. All codes to process the data and make the figures are available as a Zenodo archive (Guillaume-Castel et al., 2025).

**Acknowledgments**

R.G.C. was partly funded by the European Union Horizon Europe programme, grant agreement No 101126560; Bergen research and training program for future AI leaders across the disciplines, LEAD AI. P.C. was supported by UK Research and Innovation (UKRI) under the UK government's Horizon Europe funding Guarantee (Grant EP/Y036123/1). P.C. was additionally supported through UK Natural Environmental Research Council Grants NE/V012045/1 and NE/T006250/1. B.M. was supported by the ESA Climate space Programme under the Cross-ECV project MOTECUSOMA and by the CNES TOSCA project for the use of Sentinel 6 data. J.D. has received funding from the European Union's Horizon 2020 research and innovation programme under the Marie Skłodowska-Curie grant agreement No 101151904. We thank Aakash Manapat and two anonymous reviewers for insightful comments and discussions.

## References

Abdi, H. (2010). Partial least squares regression and projection on latent structure regression (PLS regression). *WIREs Computational Statistics*, *2*(1), 97–106. https://doi.org/10.1002/wics.51

Alessi, M. J., & Rugenstein, M. A. A. (2023). Surface temperature pattern scenarios suggest higher warming rates than current projections. *Geophysical Research Letters*, *50*(23), e2023GL105795. https://doi.org/10.1029/2023GL105795

Andrews, T., & Webb, M. J. (2018). The dependence of global cloud and lapse rate feedbacks on the spatial structure of tropical Pacific warming. *Journal of Climate*, *31*(2), 641–654. https://doi.org/10.1175/JCLI-D-17-0087.1

Armour, K. C. (2017). Energy budget constraints on climate sensitivity in light of inconstant climate feedbacks. *Nature Climate Change*, *7*(5), 331–335. https://doi.org/10.1038/nclimate3278

Armour, K. C., Proistosescu, C., Dong, Y., Hahn, L. C., Blanchard-Wrigglesworth, E., Pauling, A. G., et al. (2024). Sea-surface temperature pattern effects have slowed global warming and biased warming-based constraints on climate sensitivity. *Proceedings of the National Academy of Sciences*, *121*(12), e2312093121. https://doi.org/10.1073/pnas.2312093121

Ashok, K., Behera, S. K., Rao, S. A., Weng, H., & Yamagata, T. (2007). El Niño Modoki and its possible teleconnection. *Journal of Geophysical Research*, *112*(C11), C11007. https://doi.org/10.1029/2006JC003798

Bloch-Johnson, J., Rugenstein, M. A. A., Alessi, M. J., Proistosescu, C., Zhao, M., Zhang, B., et al. (2024). The Green's function model intercomparison project (GFMIP) protocol. *Journal of Advances in Modeling Earth Systems*, *16*(2), e2023MS003700. https://doi.org/10.1029/2023MS003700

Capotondi, A., Wittenberg, A. T., Kug, J.-S., Takahashi, K., & McPhaden, M. J. (2020). ENSO diversity. In *El niño southern oscillation in a changing climate* (pp. 65–86). American Geophysical Union (AGU). https://doi.org/10.1002/9781119548164.ch4

Ceppi, P., & Fueglistaler, S. (2021). The El niño–southern oscillation pattern effect. *Geophysical Research Letters*, *48*(21), e2021GL095261. https://doi.org/10.1029/2021GL095261

Ceppi, P., Myers, T. A., Nowack, P., Wall, C. J., & Zelinka, M. D. (2024). Implications of a pervasive climate model bias for low-cloud feedback. *Geophysical Research Letters*, *51*(20), e2024GL110525. https://doi.org/10.1029/2024GL110525

Chao, L., Muller, J. C., & Dessler, A. E. (2022). Impacts of the unforced pattern effect on the cloud feedback in CERES observations and climate models. *Geophysical Research Letters*, *49*(2), e2021GL096299. https://doi.org/10.1029/2021GL096299

Davis, L. L. B., Thompson, D. W. J., Rugenstein, M., & Birner, T. (2024). Links between internal variability and forced climate feedbacks: The importance of patterns of temperature variability and change. *Geophysical Research Letters*, *51*(24), e2024GL112774. https://doi.org/10.1029/2024GL112774

Dessler, A. E. (2020). Potential problems measuring climate sensitivity from the historical record. *Journal of Climate*, *33*(6), 2237–2248. https://doi.org/10.1175/jcli-d-19-0476.1

Dieppois, B., Capotondi, A., Pohl, B., Chun, K. P., Monerie, P.-A., & Eden, J. (2021). ENSO diversity shows robust decadal variations that must be captured for accurate future projections. *Communications Earth & Environment*, *2*(1), 1–13. https://doi.org/10.1038/s43247-021-00285-6

Dong, Y., Armour, K. C., Proistosescu, C., Andrews, T., Battisti, D. S., Forster, P. M., et al. (2021). Biased estimates of equilibrium climate sensitivity and transient climate response derived from historical CMIP6 simulations. *Geophysical Research Letters*, *48*(24), e2021GL095778. https://doi.org/10.1029/2021gl095778

Dong, Y., Proistosescu, C., Armour, K. C., & Battisti, D. S. (2019). Attributing historical and future evolution of radiative feedbacks to regional warming patterns using a green's function approach: The preeminence of the Western Pacific. *Journal of Climate*, *32*(17), 5471–5491. https://doi.org/10.1175/JCLI-D-18-0843.1

Forster, P., Storelvmo, T., Armour, K., Collins, W., Dufresne, J.-L., Frame, D., et al. (Eds.), Climate change 2021: The physical science basis. Contribution of working group I to the sixth assessment report of the intergovernmental panel on climate change. Cambridge, UK and New York, NY, USA: Cambridge University Press. https://doi.org/10.1017/9781009157896.009

Fueglistaler, S. (2019). Observational evidence for two modes of coupling between sea surface temperatures, tropospheric temperature profile, and shortwave cloud radiative effect in the tropics. *Geophysical Research Letters*, *46*(16), 9890–9898. https://doi.org/10.1029/2019GL083990

Geng, T., Cai, W., Wu, L., Santoso, A., Wang, G., Jing, Z., et al. (2022). Emergence of changing central-Pacific and eastern-Pacific El Niño-Southern oscillation in a warming climate. *Nature Communications*, *13*(1), 6616. https://doi.org/10.1038/s41467-022-33930-5

Guillaume-Castel, R., Ceppi, P., Dorrington, J., & Meyssignac, B. (2025). ENSO diversity explains interannual variability of the pattern effect [dataset]. *Zenodo*. https://doi.org/10.5281/zenodo.17186228

Guillaume-Castel, R., & Meyssignac, B. (2025). Quantifying the influence of the sea surface temperature pattern effect on transient global warming. *Journal of Climate*, *38*(14), 3417–3435. https://doi.org/10.1175/JCLI-D-24-0229.1

Hou, M., & Tang, Y. (2022). Recent progress in simulating two types of ENSO–from CMIP5 to CMIP6. *Frontiers in Marine Science*, *9*, 986780. https://doi.org/10.3389/fmars.2022.986780

Huang, B., Thorne, P. W., Banzon, V. F., Boyer, T., Chepurin, G., Lawrimore, J. H., et al. (2017a). Extended reconstructed sea surface temperature, version 5 (ersstv5): Upgrades, validations, and intercomparisons. *Journal of Climate*, *30*(20), 8179–8205. https://doi.org/10.1175/jcli-d-16-0836.1

Huang, B., Thorne, P. W., Banzon, V. F., Boyer, T., Chepurin, G., Lawrimore, J. H., et al. (2017b). NOAA extended reconstructed sea surface temperature (ERSST), version 5 [Dataset]. Retrieved from https://www.ncei.noaa.gov/access/metadata/landing-page/bin/iso?id=gov.noaa.ncdc:C00927

Ishii, M., Shouji, A., Sugimoto, S., & Matsumoto, T. (2005). Objective analyses of sea-surface temperature and marine meteorological variables for the 20th century using ICOADS and the Kobe collection. *International Journal of Climatology*, *25*(7), 865–879. https://doi.org/10.1002/joc.1169

Kao, H.-Y., & Yu, J.-Y. (2009). Contrasting eastern-pacific and central-pacific types of ENSO. *Journal of Climate*, *22*(3), 615–632. https://doi.org/10.1175/2008JCLI2309.1

Loeb, N. G., Doelling, D. R., Wang, H., Su, W., Nguyen, C., Corbett, J. G., et al. (2018). Clouds and the earth's radiant energy system (CERES) energy balanced and filled (EBAF) top-of-atmosphere (TOA) edition-4.0 data product. *Journal of Climate*, *31*(2), 895–918. https://doi.org/10.1175/jcli-d-17-0208.1

Loeb, N. G., Thorsen, T. J., Norris, J. R., Wang, H., & Su, W. (2018). Changes in earth's energy budget during and after the "pause" in global warming: An observational perspective. *Climate*, *6*(3), 62. https://doi.org/10.3390/cli6030062

Lutsko, N. J., & Takahashi, K. (2018). What can the internal variability of CMIP5 models tell us about their climate sensitivity? *Journal of Climate*, *31*(13), 5051–5069. https://doi.org/10.1175/JCLI-D-17-0736.1

Meyssignac, B., Chenal, J., Loeb, N., Guillaume-Castel, R., & Ribes, A. (2023). Time-variations of the climate feedback parameter are associated with the Pacific Decadal oscillation. *Communications Earth & Environment*, *4*(1), 1–10. https://doi.org/10.1038/s43247-023-00887-2

Meyssignac, B., Guillaume-Castel, R., & Roca, R. (2023). Revisiting the global energy budget dynamics with a multivariate Earth energy balance model to account for the warming pattern effect. *Journal of Climate*, *36*(23), 8113–8126. https://doi.org/10.1175/JCLI-D-22-0765.1

Morice, C. P., Kennedy, J. J., Rayner, N. A., Winn, J. P., Hogan, E., Killick, R. E., et al. (2021). An updated assessment of near-surface temperature change from 1850: The HadCRUT5 data set. *Journal of Geophysical Research: Atmospheres*, *126*(3), e2019JD032361. https://doi.org/10.1029/2019jd032361

Proistosescu, C., Donohoe, A., Armour, K. C., Roe, G. H., Stuecker, M. F., & Bitz, C. M. (2018). Radiative feedbacks from stochastic variability in surface temperature and radiative imbalance. *Geophysical Research Letters*, *45*(10), 5082–5094. https://doi.org/10.1029/2018GL077678

Ren, H.-L., & Jin, F.-F. (2011). Niño indices for two types of ENSO. *Geophysical Research Letters*, *38*(4), L04704. https://doi.org/10.1029/2010GL046031

Rugenstein, M., Van Loon, S., & Barnes, E. A. (2025). Convolutional neural networks trained on internal variability predict forced response of TOA radiation by learning the pattern effect. *Geophysical Research Letters*, *52*(4), e2024GL109581. https://doi.org/10.1029/2024GL109581

scikit learn. (2025). Sklearn.Cross_decomposition.PLSRegression. Retrieved from https://scikit-learn.org/stable/modules/generated/sklearn.cross_decomposition.PLSRegression.html

Sherwood, S. C., Webb, M. J., Annan, J. D., Armour, K. C., Forster, P. M., Hargreaves, J. C., et al. (2020). An assessment of Earth's climate sensitivity using multiple lines of evidence. *Reviews of Geophysics*, *58*(4), e2019RG000678. https://doi.org/10.1029/2019RG000678

Stevens, B., Sherwood, S. C., Bony, S., & Webb, M. J. (2016). Prospects for narrowing bounds on Earth's equilibrium climate sensitivity. *Earth's Future*, *4*(11), 512–522. https://doi.org/10.1002/2016EF000376

Takahashi, K., Montecinos, A., Goubanova, K., & Dewitte, B. (2011). ENSO regimes: Reinterpreting the canonical and Modoki El Niño: Reinterpreting ENSO modes. *Geophysical Research Letters*, *38*(10), L10704. https://doi.org/10.1029/2011gl047364

Titchner, H. A., & Rayner, N. A. (2014). The met office Hadley centre sea ice and sea surface temperature data set, version 2: 1. Sea ice concentrations: HADISST.2.1.0.0 sea ice concentrations. *Journal of Geophysical Research: Atmospheres*, *119*(6), 2864–2889. https://doi.org/10.1002/2013JD020316

Tsuchida, K., Mochizuki, T., Kawamura, R., & Kawano, T. (2023). Interdecadal variations of radiative feedbacks associated with the El niño and southern oscillation (ENSO) in CMIP6 models. *Geophysical Research Letters*, *50*(23), e2023GL106127. https://doi.org/10.1029/2023GL106127

Van Loon, S., Rugenstein, M., & Barnes, E. A. (2025). Reanalysis-based global radiative response to sea surface temperature patterns: Evaluating the Ai2 climate emulator. *arXiv*. https://doi.org/10.48550/arXiv.2502.10893

Wills, R. C. J., Armour, K. C., Battisti, D. S., Proistosescu, C., & Parsons, L. A. (2021). Slow modes of global temperature variability and their impact on climate sensitivity estimates. *Journal of Climate*, *34*(21), 8717–8738. https://doi.org/10.1175/JCLI-D-20-1013.1

Xie, S.-P., Kosaka, Y., & Okumura, Y. M. (2016). Distinct energy budgets for anthropogenic and natural changes during global warming hiatus. *Nature Geoscience*, *9*(1), 29–33. https://doi.org/10.1038/ngeo2581

Zhang, B., Zhao, M., & Tan, Z. (2023). Using a green's function approach to diagnose the pattern effect in GFDL AM4 and CM4. *Journal of Climate*, *36*(4), 1105–1124. https://doi.org/10.1175/JCLI-D-22-0024.1

Zhou, C., Zelinka, M. D., Dessler, A. E., & Wang, M. (2021). Greater committed warming after accounting for the pattern effect. *Nature Climate Change*, *11*(2), 1–5. https://doi.org/10.1038/s41558-020-00955-x

Zhou, C., Zelinka, M. D., & Klein, S. A. (2017). Analyzing the dependence of global cloud feedback on the spatial pattern of sea surface temperature change with a Green's function approach. *Journal of Advances in Modeling Earth Systems*, *9*(5), 2174–2189. https://doi.org/10.1002/2017MS001096